Scientia Iranica B (2013) 20(6), 1812–1823

Sharif University of Technology
Scientia Iranica
Transactions B: Mechanical Engineering
www.scientiairanica.com

Research Note

Finite volume-lattice Boltzmann modeling of time-dependent flows

A. Zarghami[a,*] and P. Omidvar[b]

a. *Department of Engineering, Science and Research Branch, Islamic Azad University, Fars, Iran.*
b. *Department of Mechanical Engineering, The University of Yasouj, Yasouj, Iran.*

Received 18 September 2011; received in revised form 18 December 2012; accepted 12 March 2013

KEYWORDS
LBM;
Finite volume;
Time-dependent flow;
Circular cylinder;
Mixing layer.

Abstract. In this paper, a stable finite volume formulation of the lattice Boltzmann method is used to study time-dependent flows. For simulation purposes, a cell-centered scheme is implemented to discretize the convection operator and weighting factors are used as flux correctors to enhance the stability. Also, additional lattices at the edge of each boundary cell are used, which allow a much better description of the actual geometrical shape. Compared with previous finite volume formulations, the proposed approach resulted in a wider domain of stability and faster convergence. The scheme is validated through simulations on flow over a circular cylinder and mixing layer flow. The results show that the method is a promising scheme for simulating time-dependent flows.

© 2013 Sharif University of Technology. All rights reserved.

1. Introduction

In recent years, there has been considerable research in developing and expanding the Lattice Boltzmann Method (LBM) for solving different fluid dynamics problems. The LBM was first introduced by McNamara and Zanetti [1] as an improvement to the method of Lattice Gas Automata (LGA). Later, it was shown that the Lattice Boltzmann Equation (LBE) could be derived from the continuous Boltzmann equation by choosing an appropriate set of discrete velocities, based on some special discretization schemes. This approach helped for better understanding of the basis of LBM, and provided a solid theoretical foundation for LBM [2].

The fundamental idea of the LBM is to construct simplified kinetic models that incorporate the essential physics of microscopic or mesoscopic processes, so that the macroscopic averaged properties obey the desired macroscopic equations. The basic premise for using these simplified kinetic-type methods for macroscopic fluid flow is that the macroscopic dynamics of a fluid are the result of the collective behavior of many microscopic particles in the system and that macroscopic dynamics are not sensitive to the underlying details in microscopic physics. By developing a simplified version of the kinetic equation, it is not required to solve complicated kinetic equations such as the full Boltzmann equation, and it is not needed to follow each particle as in molecular dynamics simulations [2].

LBM is based on a microscopic picture but focuses on the averaged macroscopic behavior of the fluid. That gives simplicity of implementation, a clear physical picture and fully parallel algorithm. Briefly, the advantages of the LBM over the conventional CFD schemes can be summarized as:

I) Simple explicit algorithm;

II) Parallelization capability for doing massively parallel simulations;

III) Ability to handle complex geometries;

*. *Corresponding author. Tel.: +98 7284692101-4*
E-mail addresses: a.zarghami@fsriau.ac.ir (A. Zarghami); pourya.omidvar@gmail.com (P. Omidvar)

IV) Robust simulations for complex fluids and etc. [3].

The standard BGK approximation of LBM, based on Single-Relaxation-Time (SRT), was introduced by Qian et al. [4], the latter being based on the original idea of Bhatnagar et al. (1954) [2]. Due to its extreme simplicity, the lattice BGK equation has become the most popular LB model. But, the standard BGK-LBM suffers from numerical instabilities that can induce a local blowup of the computation [5]. So, in recent years, intensive studies on stability analysis regarding different lattice Boltzmann models have been carried out by various researchers.

The Multiple-Relaxation-Time (MRT) model [6,7], based on the original matrix, a formulation of the LBM, has been proposed as an alternative to the standard BGK model by D'Humieres [6]. In this model, the collision step is performed in moment space, whereas the propagation step is done in discrete velocity space. The MRT models are considerably more stable than the standard SRT model and overcome some obvious defects in the standard BGK model, such as the fixed ratio between the kinematic and bulk viscosities [8]. However, the stability properties of the MRT-LB models are still not satisfactory [9]. Thus, the MRT-LBM has been persistently pursued, and much progress has been made [10].

Recently, in order to improve the stability and accuracy of the LB schemes, with regards to rough mesh, the Entropic Lattice Boltzmann Method (ELBM) has been developed. The goal of this approach, proposed by Ansumali et al. [11-13], is construction of a scheme that: I) satisfies the Boltzmann H-theorem and II) shows a higher non-linear stability. In this approach, an entropy function is defined for the kinetic equation and it is ensured, at each iteration step, that the entropy of the system remains non-decreasing (Boltzmann H-theorem). This simple idea renders the method thermodynamically consistent and makes the simulations non-linearly stable. However, ELBM were known only on highly symmetric lattices, such as the 27 velocity lattice (D_3Q_{27}). So, in order to increase the speed of simulations, it is required that the number of discrete velocities be reduced [14].

Another limitation of the standard LBM is the use of uniform Cartesian grids. This limitation is particularly severe in many practical applications where the complex geometry of boundaries cannot be well fitted by regular lattices. In order to overcome such limitation and increase computational efficiency, locally embedded uniform grids [15,16] and interpolated grid stretching [17,18] have been proposed.

In locally embedded uniform grids, Cartesian meshes are used and grid spacing is divided by an integer (or level of refinement) to the next refined grid level. In this scheme, refined uniform grids and the main coarse grids live on different space and time scales. The consequence is that one needs to perform less time steps on the coarse grid than on the fine grid, because also, time is refined locally [19]. In the interpolated grid stretching scheme, interpolations are used at the interface between two connected meshes of different grid spacing and at solid boundaries [20]. With the interpolated grid stretching method, one can use the simple bounce-back boundary conditions with body-fitted meshes. However, this method requires an extra computational effort for interpolation at every time step and it also has a strict restriction on the selection of interpolation points, which requires upwind 9 points for 2D problems and upwind 27 points for 3D problems if a structured mesh is used [21].

Among recent advances in LB research to handle complex flows, a particularly remarkable option is represented by changing the solution procedure from the original 'stream and collide' to a Finite Volume (FV) formulation. The first attempt to combine the FV method with LBM is attributed to Nannelli and Succi [22]. They obtained a FV-LBM for the volume-averaged coarse-grain distribution function, starting from the discrete velocity Boltzmann equation. Peng et al. proposed a cell-vertex finite volume scheme [23]. This method allows for an arbitrary decomposition of the computational domain into triangular or quadrilateral elements, with no structural limitations for the mesh. Using the mapped or non-uniform grid for the structured grid is another advantage of this method, which results in a decrease in the number of grid nodes and iterations for desired accuracy.

For the FV-LB methods, one needs to select efficient approaches, such as upwind schemes, to do numerical discretization, in order to get a stable solution [24]. Numerical research has shown that these methods have good capabilities in real applications. However, most of the presented FV schemes have several drawbacks with respect to numerical stability [25].

The primary motivation of this research is to develop a stable FV formulation of the LBM to study global time-dependent flows. The introduction of upwind weighting factors allows overcoming instability and accelerating the convergence process. In this paper, we extended the method to simulate the flow past a circular cylinder and mixing layer flow to study the instability of these flows. The abundant literature on these classical flow problems allows us to carry out extensive benchmarking for this new formulation. Here, we first describe the LBE, the proposed cell-centered finite-volume scheme and boundary conditions. Then, the computational results are presented, followed by the concluding remarks.

2. Lattice Boltzmann-finite volume formulation

2.1. Discrete lattice Boltzmann equation

The Boltzmann equation discretized in velocity space, and the collision term modeled with BGK [2] approximation, is usually written in the following differential form:

$$\frac{\partial f_i}{\partial t} + \vec{v}_i.\nabla f_i = -\frac{1}{\tau}\left(f_i - f_i^{eq}\right) \quad i = 1, ..., n, \tag{1}$$

where n is the number of different velocities in the model, f^{eq} is the particle equilibrium distribution function associated with motion along the i^{th} direction in velocity space, $\vec{v}_i$ is the velocity in the i^{th} direction, τ is the relaxation time and the right hand side of the equation is the collision operator.

The discrete velocities and the equilibrium distribution functions must be chosen appropriately, such that the mass and momentum are conserved and some symmetry requirements are satisfied. Here, we choose the 2D nine-bit (D_2Q_9) model with the equilibrium distribution function defined as:

$$f_i^{eq}(\vec{x}, t) = w_i\rho \left[c_1 + c_2(\vec{v}_i.\mathbf{u}) + c_3(\vec{v}_i.\mathbf{u})^2 + c_4(\mathbf{u}.\mathbf{u})\right], \tag{2}$$

where $c_1 = 1, c_2 = 1/c_s^2, c_3 = 1/2c_s^4, c_4 = -1/2c_s^2$ and w_i is the weighting factor and equals $4/9$ for $i = 0$, $1/9$ for $i = 1 \sim 4$ and $1/36$ for $i = 5 \sim 8$. The discrete velocities are given by $\vec{v}_o = 0$ and $\vec{v}_i = \lambda_i(\cos\theta_i, \sin\theta_i)$ with $\lambda_i = 1, \theta_i = (i-1)\pi/2$ for $i = 1 \sim 4$ and $\lambda_i = \sqrt{2}, \theta_i = (i-5)\pi/2 + \pi/4$ for $i = 5 \sim 8$ and $c_s = c/\sqrt{3} = 1/\sqrt{3}$ is the speed of sound in the model [2]. The macroscopic density, ρ and velocity, $\mathbf{u}$, of the fluid are determined by $\rho = \Sigma_i f_i$ and $\rho\mathbf{u} = \Sigma_i f_i \vec{v}_i$, respectively. Also, the corresponding kinematic shear viscosity isrelated to the relaxation time by $v = c_s^2\tau$, and macroscopic pressure is given by $p = c_s^2\rho$ [25].

2.2. FV formulation of LBM

According to Figure 1, the integration of the first term in Eq. (1), based on the cell-centred finite-volume scheme, is approximated as:

$$\int_{abcd} \frac{\partial f_i}{\partial t} dA \approx \left[\frac{\partial f_i}{\partial t}\right]_{I,J} A_{I,J}, \tag{3}$$

where $A_{I,J}$ is the area of $abcd$. In the above equation, f_i is assumed to be constant over the area $abcd$, thus avoiding a set of equations to be solved. This is a common practice in the finite volume methods [26].

A standard integration of the second term of the left-hand side of Eq. (1) gives the flux associated with the streaming operator of the i^{th} particle distribution function through the four edges ab, bc, cd and da. As v_{ix} and v_{iy} are constant, the following equation is obtained after applying Green's theorem:

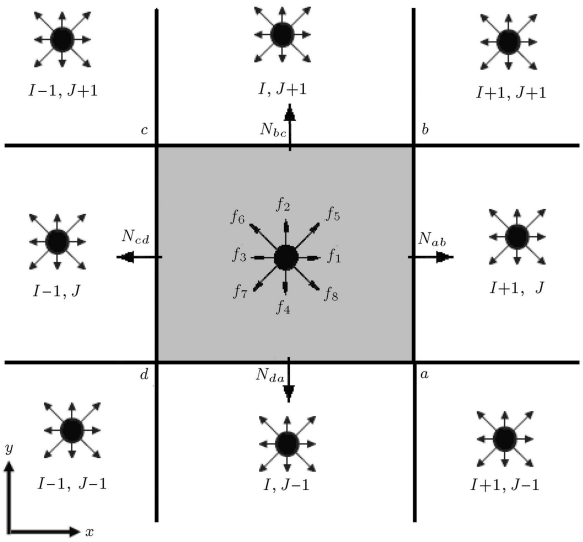

Figure 1. Schematic of the FV discretization with cell-centered lattice.

$$\begin{aligned}
\int_{abcd} v_i.\nabla f_i\, dA &= \int_{abcd} \left\{\frac{\partial(v_{ix}.f_i)}{\partial x} + \frac{\partial(f_i.v_{iy})}{\partial y}\right\} dx\, dy \\
&= \oint_{\text{around } I,J} (v_{ix}\, f_i\, dy - v_{iy}\, f_i\, dx) \\
&\approx \frac{[f_i]_{I,J} + [f_i]_{I+1,J}}{2} v_i.N_{ab} \\
&+ \frac{[f_i]_{I-1,J} + [f_i]_{I,J}}{2} v_i.N_{bc} \\
&+ \frac{[f_i]_{I,J} + [f_i]_{I,J+1}}{2} v_i.N_{cd} \\
&+ \frac{[f_i]_{I,J-1} + [f_i]_{I,J}}{2} v_i.N_{da} A.
\end{aligned} \tag{4}$$

In the above equation, $N_k = (\Delta y\bar{i} - \Delta x\bar{j})_k$ is the outward unit vector normal to the edge, and $k = ab, bc, cd, da$. This formulation is named the *flux averaging* scheme, which would diverge if the flux term be weak [27]. This could be avoided by using the divergence theorem and applying an upwind scheme. In this case, the integration of the second term of the left-hand side of Eq. (1) results as follows [24]:

$$\int_{abcd} v_i.\nabla f_i\, dA = \begin{cases} [f_i]_{I,J}\, v_i.N_{ab} & \text{if } v_i.N_{ab} \geq 0 \\ [f_i]_{I+1,J}\, v_i.N_{ab} & \text{if } v_i.N_{ab} < 0 \end{cases}$$

$$+\begin{cases}[f_i]_{I,J}\, v_i.N_{bc} & \text{if } v_i.N_{bc}\geq 0\\ [f_i]_{I,J+1}\, v_i.N_{bc} & \text{if } v_i.N_{bc}<0\end{cases}$$

$$+\begin{cases}[f_i]_{I,J}\, v_i.N_{cd} & \text{if } v_i.N_{cd}\geq 0\\ [f_i]_{I-1,J}\, v_i.N_{cd} & \text{if } v_i.N_{cd}<0\end{cases}$$

$$+\begin{cases}[f_i]_{I,J}\, v_i.N_{da} & \text{if } v_i.N_{da}\geq 0\\ [f_i]_{I,J-1}\, v_i.N_{da} & \text{if } v_i.N_{da}<0\end{cases}$$

$$\approx \sum_k \vec{v}_i.N_k(f_i)_k. \tag{5}$$

Now, the following weighting factors are employed in the convective fluxes of Eq. (1):

$$\zeta_{ab}=\frac{\Delta p_{ab}}{\sum p_{\text{horizental}}},\quad \zeta_{bc}=\frac{\Delta p_{bc}}{\sum p\ _{tvertical}},$$

$$\zeta_{cd}=\frac{\Delta p_{cd}}{\sum p_{\text{horizental}}},\quad \zeta_{da}=\frac{\Delta p_{da}}{\sum p_{\text{vertical}}}. \tag{6}$$

where:

$$\sum p_{\text{horizental}}=\sum\left(p_{I+1,J}+2p_{I,J}+p_{I-1,J}\right),$$

$$\sum p_{\text{vertical}}=\sum\left(p_{I,J+1}+2p_{I,J}+p_{I,J-1}\right),$$

and:

$$\Delta p_{ab}=p_{I+1,J}-p_{I,J},\quad \Delta p_{bc}=p_{I,J+1}-p_{I,J},$$

$$\Delta p_{cd}=p_{I,J}-p_{I-1,J},\quad \Delta p_{da}=p_{I,J}-p_{I,J-1}.$$

The idea of introducing these factors to improve numerical stability without adding artificial viscosity is related to the fact that the macroscopic pressure, p, acts as a driving force for the flow between the two cells [28]. So, according to the above relations, the convective fluxes may be written as follows:

$$\begin{aligned}S_i=\int \vec{v}_i.\nabla f_i dA \approx{}& \vec{v}_i.N_{ab}\big(\xi_{ab}[f_i]_{I,J}\\ &+(1-\xi_{ab})[f_i]_{I+1,J}\big)\\ &+\vec{v}_i.N_{bc}\big(\xi_{bc}[f_i]_{I,J}+(1-\xi_{bc})[f_i]_{I,J+1}\big)\\ &+\vec{v}_i.N_{cd}\big(\xi_{cd}[f_i]_{I,J}+(1-\xi_{cd})[f_i]_{I-1,J}\big)\\ &+\vec{v}_i.N_{da}\big(\xi_{da}[f_i]_{I,J}\big)\\ &+(1-\xi_{da}[f_i]_{I,J-1}\big).\end{aligned} \tag{7}$$

The heuristic meaning of these coefficients is to enhance transport downhill the pressure gradient and reduce it uphill [29]. Assuming a linear behavior of f_i, f_i^{eq} within internal cells, the integration of the collision term (right-side term of Eq. (1)) is performed through the following formulation:

$$\begin{aligned}Q_i\cong -\frac{A_{I,J}}{\tau}\Bigg[&\frac{1}{4}[f_i^{ne}]_{I,J}+\frac{1}{8}\Big\{[f_i^{ne}]_{I+1,J}\\ &+[f_i^{ne}]_{I,J+1}+[f_i^{ne}]_{I-1,J}+[f_i^{ne}]_{I,J-1}\Big\}\\ &+\frac{1}{16}\Big\{[f_i^{ne}]_{I+1,J-1}+[f_i^{ne}]_{I+1,J+1}\\ &+[f_i^{ne}]_{I-1,J+1}+[f_i^{ne}]_{I-1,J-1}\Big\}\Bigg],\end{aligned} \tag{8}$$

where $f_i^{ne}=f_i-f_i^{eq}$ is the non-equilibrium component of the distribution function. Note that the integration of the collision terms in boundary cells reduces to the following form:

$$Q_i\cong -\frac{A_{I,J}}{\tau}\left[(f_i)_{I,J}-(f_i^{eq})_{I,J}\right]. \tag{9}$$

As we know truncation or round-off causes error in the numerical solution of partial differential equations, the solution may go unstable in typical cases (such as flows with strong gradients) unless artificial dissipation is explicitly added to the calculation. Note that artificial dissipation is the direct result of even order derivatives in modified equation [30]. So, in flux modeling, especially at high Reynolds numbers or in the presence of strong gradients, the addition of artificial dissipation is inevitable to perform a stable simulation. Therefore, in order to damp out spurious oscillations the fourth-order artificial dissipation takes the following form:

$$\begin{aligned}\left[D^{(4)}f_i\right]_{I,J}=&\epsilon_x\cdot(\nabla\Delta)_x^2\cdot[f_i]_{I,J}\\ &+\varepsilon_y\cdot(\nabla\Delta)_y^2\cdot[f_i]_{I,J},\end{aligned} \tag{10}$$

where ε_x and ε_y are damping factors in x and y directions, respectively, and the integration over each cell is the sum of flux the time updating. These damping factors were adjusted to achieve the desired numerical stability and convergence. In Eq. (10), the fourth-order gradient operator (Nabla-Delta) was discretized in x and y directions as follows:

$$\begin{aligned}(\nabla\Delta)_x^2\cdot[f_i]_{I,J}=&[f_i]_{I+2,J}-4[f_i]_{I+1,J}+6[f_i]_{I,J}\\ &-4[f_i]_{I-1,J}+[f_i]_{I-2,J},\\ (\nabla\Delta)_y^2\cdot[f_i]_{I,J}=&[f_i]_{I,J+2}-4[f_i]_{I,J+1}+6[f_i]_{I,J}\\ &-4[f_i]_{I,J-1}+[f_i]_{I,J-2}.\end{aligned} \tag{11}$$

A modified fifth order, Runge-Kutta time differencing scheme is used to advance the computations in time [28]. Therefore, the new-time particle distribution function is calculated as follows:

$$f_i^{n+1} = f_i^n + \alpha_l \frac{\Delta t}{A_{I,J}} \left(S_i^{l-1} + Q_i^{l-1} \right), \tag{12}$$

where n denotes the time step, $\alpha_1 = 0.0695, \alpha_2 = 0.1602, \alpha_3 = 0.2898, \alpha_4 = 0.5, \alpha_5 = 1$ and $l = 1, ..., 5$.

2.3. Boundary conditions

In order to transform hydrodynamic boundary conditions to the boundary conditions for the distribution functions, additional lattices at the edge of each boundary cell are introduced. Then, boundary nodes are treated like internal nodes, except that the fluxes over boundary edges also have to be evaluated. The inlet boundary conditions at $I = 1$ are given by (see Figure 2):

$$f_1 = f_3 + 2u_{\text{in}}/3,$$

$$f_5 = f_7 + 0.5(f_4 - f_2) + u_{\text{in}}/6,$$

$$f_8 = f_6 + 0.5(f_2 - f_4) + u_{\text{in}}/6. \tag{13}$$

The above described scheme is also known as Zou and He boundary conditions, suggesting the name of the original authors proposing this idea. At the outlet boundary, i.e. $I = N_x$, the distribution functions are extrapolated as follows:

$$f_i(I = N_x, J) = 1.5 f_i(I = N_x - 1, J) - 0.5 f_i(I = N_x - 2, J). \tag{14}$$

For the free slip boundary condition (Figure 2), the unknown distribution functions are calculated as $f_8 = f_5$, $f_4 = f_2$ and $f_7 = f_6$. This implies no tangential momentum transfer to the boundary, as required for a free slip fluid motion [31]. *Wall* boundary conditions are in LB simulations usually implemented by applying the so-called *bounce-back* rule, which means that incoming particle portions are reflected back towards the nodes they came from, and which gives second-order accuracy for straight walls [21]:

$$f_6 = f_8, \; f_2 = f_4, \; f_5 = f_7. \tag{15}$$

For the arbitrary shaped solid wall, θ suggests the selection of appropriate f_is for extrapolation purposes.

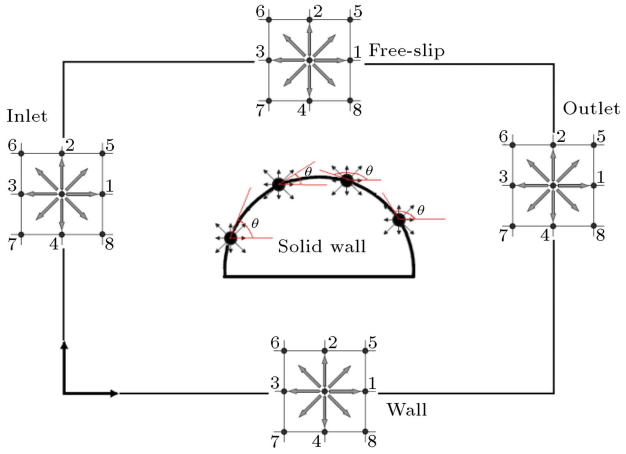

Figure 2. Physical boundaries of the solution domain and lattice model on typical boundaries.

3. Simulation results

First, we applied the model to flow over a circular cylinder and then in the second part, the results for simulating a time-dependent mixing layer flow are presented. In all cases, the results were compared with available well-documented solutions in the literature.

3.1. Flow over circular cylinder

One of the basic time-dependent problems in hydrodynamics is the flow past a circular cylinder, which has been both numerically and experimentally studied extensively in the past, thus becoming a standard benchmark problem. The flow has been numerically simulated for Reynolds number up to 150. The Reynolds number is calculated as $\text{Re} = UD/\nu, U$ being the inlet uniform velocity and D the cylinder diameter.

Figure 3(a) shows a schematic of the flow configuration and boundary conditions simulated here. The symmetry boundary conditions were used for top and bottom walls. All the simulations have been performed in a large $32D \times 16D$ domain so as to minimize the effects of boundaries on the development of the wake. To investigate grid independency, the Wake length (L) was considered at three different non-uniform grid points, $150 \times 80, 180 \times 100$, and 200×120, at Re=40. It was observed that the grid point of 200×120 was sufficiently fine to ensure a grid-independent solution for laminar flow (see Figure 3(b)). The flow is impulsively started by forcing a uniform profile at the inlet. Then, after reaching the fully periodic solution, we measure and report the length of the wake behind the cylinder, the separation angle and the drag coefficient.

The convergence criterion is applied to the velocity field to ensure that the convergence happens. If the velocity satisfies this criterion, the program code will go to the next step and the iterations will continue. Generally, the proper equation defines the investigation of the convergence situation for the numerical methods. In other words, the error functions are used for assurance that a parameter-like velocity converges. Here, a relative velocity error is applied as follows:

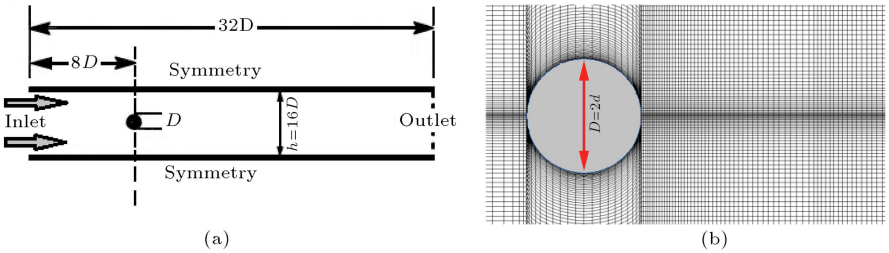

Figure 3. (a) Flow configuration for simulation of flow past a cylinder placed symmetrically in a planar channel. (b) Mesh grids around circular cylinder.

Table 1. Relative velocity error for different flux modeling schemes (finite volume formulation).

Flux modeling scheme	Relative velocity error			
	Re = 20	Re = 40	Re = 80	Re = 100
Averaging scheme (Eq. (4))	1.1E-04	4.5E-04	Diverged	Diverged
Upwind scheme (Eq. (5))	6.4E-04	3.3E-03	8.7E-03	Diverged
Pressured based scheme (Eq. (7))	4.8E-05	4.6E-05	4.6E-05	4.5E-05
Averaging scheme with artificial dissipation ($\varepsilon_x = \varepsilon_y = 5$)	5.9E-05	6.4E-05	7.3E-05	diverged
Pressured based scheme with artificial dissipation ($\varepsilon_x = \varepsilon_y = 5$)	1.4E-05	1.5E-05	1.7E-05	2.5E-05

$$E^{n+1} = \frac{\sum_{I,J} \left| \sqrt{\left(u_{I,J}^2 + v_{I,J}^2\right)^{n+1}} - \sqrt{\left(u_{I,J}^2 + v_{I,J}^2\right)^{n}} \right|}{\sum_{I,J} \left| \sqrt{\left(u_{I,J}^2 + v_{I,J}^2\right)^{n+1}} \right|}, \quad (16)$$

where n and $n+1$ indicate the reference and under test condition, respectively. Also, u and v are stream-wise and span-wise components of the velocity, respectively. Table 1 compares the relative velocity error of the flow over a circular cylinder for different flux modeling schemes. In this table, results are presented in iteration equal to 20000. As seen, applying the pressure based factors enabled us to reach a more stable solution in the mentioned Reynolds numbers. Also, a better convergence was achieved by adding the artificial dissipation term. This led to an improvement in the stability and accuracy of the numerical scheme and reduction in iteration steps.

Another parameter which has an influence on the accuracy of the solution is compressibility error, which is related to the fact that the LBE recovers the Navier-Stokes for weakly-compressible flows (Ma<<1). In other words, The LB model is a quasi-compressible fluid solver. This means that it enters a slightly compressible regime to solve the pressure equation of the fluid. Compressibility effects do, however, impact numerical accuracy. As these effects scale like the square Mach-number, Ma^2, they are kept under control by keeping the Mach number low. The Mach number is nothing else than U_{in}/c_s, which means that it is proportional to the velocity in the lattice unit, U_{in}. So, in all simulations, inlet velocity U_{in} was set to 0.03 and, consequently, Mach number was obtained equal to Ma= $0.03 \times \sqrt{3} \cong 0.05$.

The results of Figure 4 show the time history of the relative velocity error by adding the artificial dissipation to *flux averaging* and *pressure based*

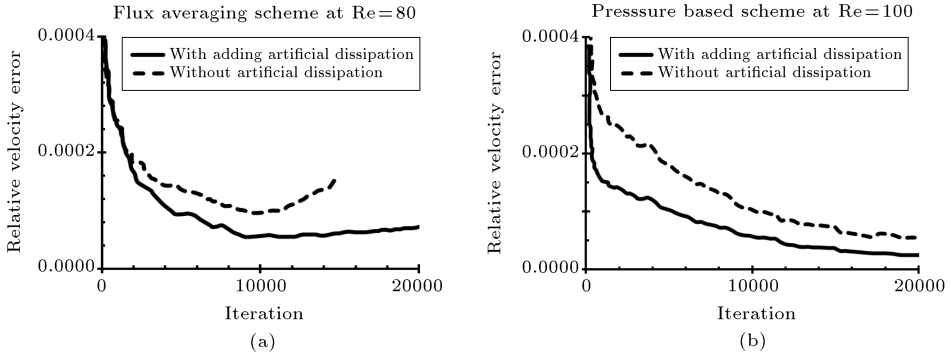

Figure 4. Effect of artificial dissipation ($\varepsilon_x = \varepsilon_y = 5$) in numerical convergence of the flow over a circular cylinder: (a) Flux averaging scheme at Re = 80; and (b) pressure based scheme at Re = 100.

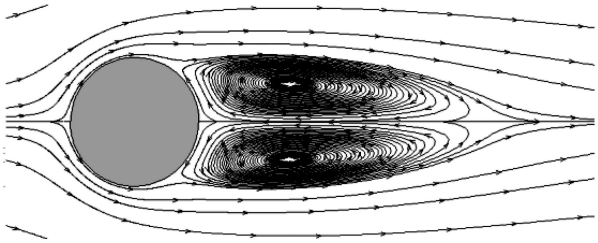

Figure 5. Streamline plot of flow past circular cylinder at Re = 40.

Table 2. Comparison of geometrical and dynamical parameters at Re = 40: L = length of wake, d = cylinder radius, θ_s = separation angle.

Authors	L/d	θ_s	C_D
Coutanceau and Bouard [32]	4.26	53.5	-
Dennis and Chang [33]	4.69	53.8	1.552
Nieuwstadt and Keller [34]	4.357	53.34	1.550
He and Doolen [35]	4.49	52.84	1.499
Patil and Lakshmisha [36]	4.284	52.74	1.558
Fornberg [37]	4.48	-	1.5
Calhoun [38]	4.36	-	1.62
Ye et al. [39]	4.54	-	1.52
Ubertini et al. [40]	-	-	1.56
Present work	4.47	52.8	1.551

schemes. Hence, a better convergence was achieved. To conclude, applying the pressure-biasing factors and artificial dissipation term enabled us to overcome some shortcomings, especially the numerical instability of finite volume formulations of the lattice Boltzmann method.

Details of the flow path behind the cylinder at the Re=40 are shown in Figure 5. We see that the two vortices in the streamline plot are perfectly aligned, indicating that the flow is stable. Table 2 compares the present numerical results with previous experimental and computational results [32-40]. In particular, the length of the wake behind the cylinder, the separation angle and the drag coefficient computed with the present method are in good agreement with the corresponding values available in the literature.

It is generally accepted that the wake of a cylinder immersed in a free-stream first becomes unstable to perturbations at a critical Reynolds number of about Re = 46 ± 1[39]. Above this Reynolds number, a small asymmetric perturbation in the near wake will grow in time and lead to an unsteady wake and Von Karman vortex shedding. This is indeed what we find for our simulation at Re = 62, which has been carried out on a 320 × 240 non-uniform mesh. Figure 6 shows the behavior of the relative velocity error at Re = 60, 62 and 100. For Reynolds higher than 62, we see that the

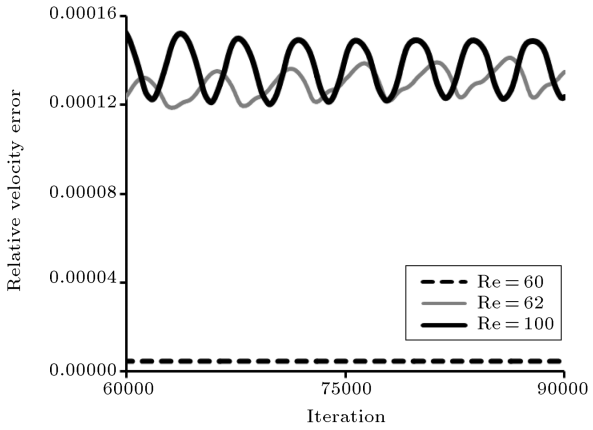

Figure 6. Behavior of velocities residuals at Re = 60, 62 and 100.

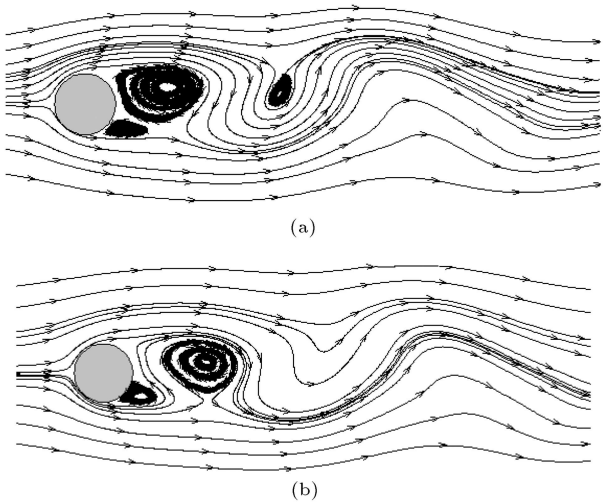

Figure 7. Streamline plot of flow past circular cylinder: (a) Re = 100; and (b) Re = 150.

behavior of relative velocity error is periodic. Figure 7 shows a plot of the streamline pattern for Re = 100 and 150. The vortices in the streamline plot have begun to slide past one another, indicating the onset of vortex shedding, and the zero-contour level has begun to warp. The characteristic vortex shedding is clearly visible in the plots.

In order to investigate the effect of Mach number on the accuracy of simulation, the time-dependent behavior of drag coefficient, C_D, at different Mach numbers and Re = 100, are plotted in Figure 8. Results are compared with the incompressible finite difference solution of Calhoun [38]. From these simulations, it is obvious that the difference between Ma = 0.03 and the incompressible solution is very low. In this work, values of drag coefficient differ from the incompressible solution by a small discrepancy of about 0.86% in the whole periodic region. The difference between the incompressible result and the case for Ma = 0.08 is equal to 8.8% for average values in the periodic

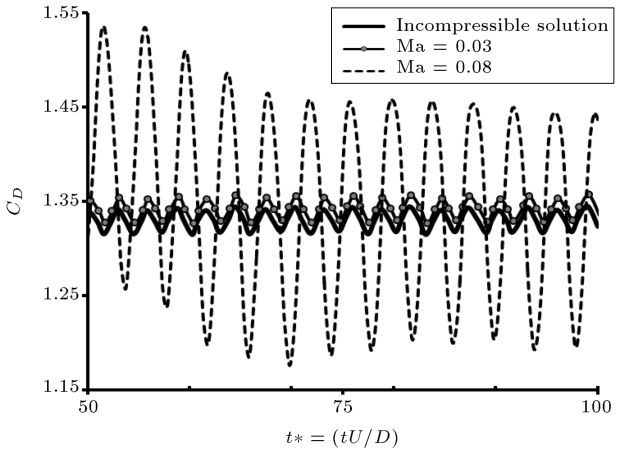

Figure 8. Time-dependent drag coefficient at Re = 100 and different Mach numbers. Results compared with incompressible result of Calhoun [38].

Table 3. Comparison of drag coefficient for unsteady flow at Re = 100.

Authors	C_D
Calhoun [38]	1.330
Ding et al. [41]	1.391
Liu et al. [42]	1.350
Braza et al. [43]	1.364
Present work	1.310

region. Therefore, it is shown that the results of the lattice Boltzmann simulation have significant dependence on the chosen Mach number. Thus, the effect of Mach number on the accuracy of the solution should be considered in simulations using LB methods. Table 3 lists quantitative comparisons for the drag coefficient.

To determine if we are getting the proper shedding frequency, we compute the non-dimensional shedding frequency, or Strouhal number, given by $\mathrm{St} = f_s D/U$, where f_s is the shedding frequency. To compute the shedding frequency, the periodic evolution of the drag coefficient was used. We estimate a non-dimensional Strouhal number of about 0.161 for Re = 100. By comparison, Ding et al. [41] reports a value of St = 0.166, and Liu [42] reports a value of St = 0.164.

Figure 9 represents the St-Re relation for different schemes available in the literature. One can clearly find that, although the results from the different schemes deliver very different values for the Strouhal number, they all have something in common. The reason is that both Reynolds number and Strouhal number are functions of the inflow uniform velocity, U. Generally, the quantitative agreement between our results and other numerical/experimental results is satisfactory, and we conclude that our scheme is correctly capturing the transition from steady to unsteady flow.

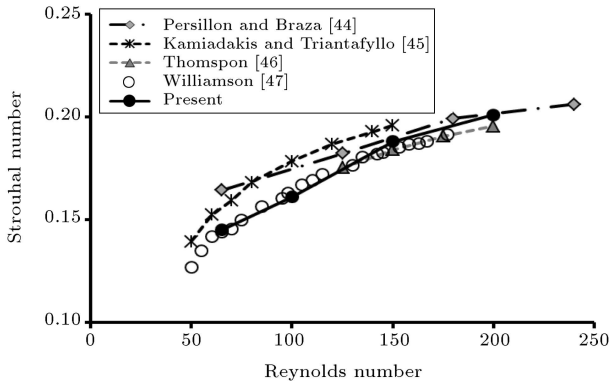

Figure 9. Graphical presentation (St-Re) of former studies compared [44-47] with the results from the present works.

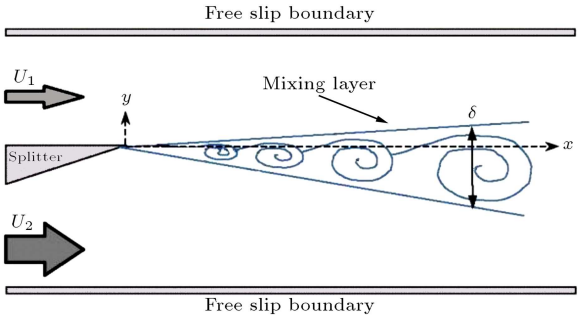

Figure 10. Schematic of mixing layer flow. Fast side refers to lower stream and slow side refers to upper stream and δ refers to the thickness of the mixing layer.

3.2. Time-dependent mixing layer flow

The plane mixing layer is characterized by the merging of two initially unperturbed parallel flow streams with velocities U_1 and U_2 (see Figure 10). Downstream of the confluence, the two streams exchange momentum as they come into intimate contact with each other. The mixing layer itself is defined by the region in which this merging process is occurring. In this study, the computational domain is $L_x = L_y = 80\delta$, where δ is the theoretical thickness of the layer in $x = L_x$ [48]. The theoretical thickness of the mixing layer flow is calculated according to analytical solution, whereas it is estimated based on the inlet velocity profile for mixing layer flows. The system size of the mesh grid is 261×521. In the y direction, an equally spaced grid is used in the mixing layer thickness i.e. for $35\delta < y < 45\delta$, and then the grid is stretched on both sides. Also, in the x direction, the grid is uniform between $0 < x < 5\delta$ and then stretched.

The flow is initially at rest (zero speed) and is impulsively started by forcing a hyperbolic profile, such as $U_{\mathrm{inlet}}(y) = 0.5\{(1/\lambda) + \tanh(y)\}$ at the inlet where $\lambda = [U_2 - U_1]/[U_1 + U_2]$ represents a measure for the intensity of the layer shearing. The flow has been numerically simulated for a Reynolds number equal to $\mathrm{Re} = \Delta U\delta/\nu = 300$, where $\Delta U = U_2 - U_1$.

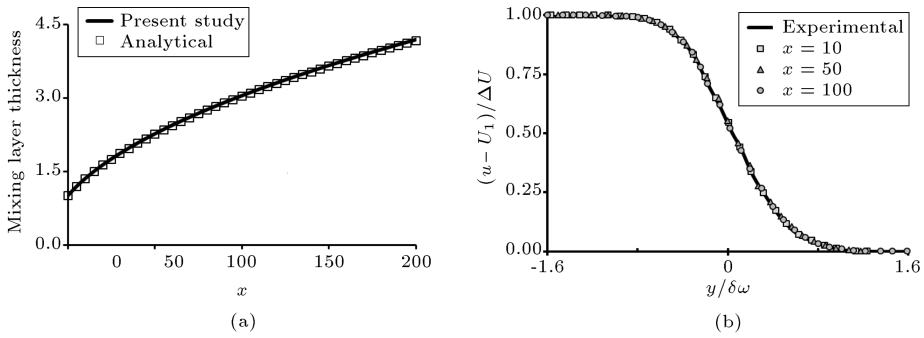

Figure 11. (a) Mixing layer thickness at Re = 300. Curve fit using $\delta_\omega = 0.2875\sqrt{x + 12.371}$. (b) The variation of the normalized u-component velocity.

When the flow gets steady, the results of the simulation essentially display a laminar growth of the boundary layer. Figure 11(a) illustrates the stream-wise growth of the mixing layer thickness, $\delta_\omega = 1/(\partial\bar{U}/\partial y)_{\max}$ where the average layer speed, $\bar{U} = 0.5(U_1 + U_2)$, is set at 1.5. A square-root relationship fit to these computed results is shown in the graph reported in Figure 11(a). The layer is respondent with classical laminar, square-root growth characteristics [49].

A dimensionless variable that is written as a function of a dimensionless transverse coordinate is called self-similar if the function does not change with the downstream position. Results in self-similar coordinates for the mixing layer were also investigated. The principle of self-similarity as a representation of moving equilibrium was introduced by Townsend [50]. Free shear layers provide an excellent example of this equilibrium, and they form one class of canonical laminar and turbulent flow fields.

In order to verify our results, the present numerical results are compared to the experimental data of Oster and Wygnanski [51]. Non-dimensional time-averaged stream-wise velocities obtained by a statistical method at different stations are shown in Figure 11(b). This figure clearly shows that the self-similarity of the mixing layer is obtained using LBM, and indicates that the mixing layer is a flow with a self-preserving state.

Now, in order to investigate the unsteady mixing layer flow, the inlet velocity component is superimposed by some time-dependent perturbations. The perturbations are introduced in the form of a traveling wave. The perturbation, which consists of a combination of linear Eigen-functions obtained from the linear stability calculations, is specified for the inflow boundary condition. In other words:

$$v(x, y, t) = A \cdot \text{Real}[V(y)e^{i(-\omega t)}], \tag{17}$$

where $V(y)$ is the velocity Eigen-function corresponding to the most amplified mode of the two-dimensional Orr-Sommerfeld equation, and A is the amplitude of the two-dimensional forcing which corresponds to the fundamental frequency [52]. Figure 12 illustrates the time traces of the stream-wise component of velocity at a selected location in the layer. The figures clearly indicate that the response of the layer is very periodic, which is due to the periodic forcing imposed at the inlet plane of the layer. The peak-to-peak time lapse in these curves provides evidence of the passage of a structure. This time lapse, Δt, together with an assumed advection speed for these structures of $\bar{U}$, allows estimation of the scale of a structure.

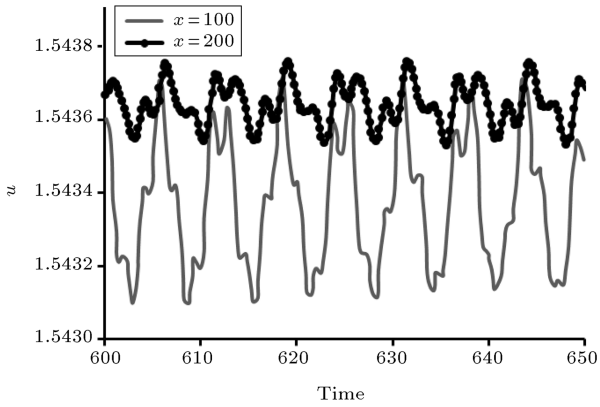

Figure 12. Velocity time histories at centerline for the u component at stream-wise location, $x = 100$ and 200.

The mean field statistics for the stream-wise velocity component is illustrated in Figure 13(a). Clearly, these results are not representative of a self-similar layer. The lack of self-similarity is apparently as a result of the forcing imposed at the inlet plane. As the flow goes downstream, the distributions become closer together. This is indicating that the flow enters the self-similar region. The Reynolds stress statistics, $\sqrt{\overline{u'v'}}/\Delta U$, obtained from this simulation are illustrated in Figure 13(b). Again, these profiles do not exhibit self-similar behavior. The distributions are more likely to collapse on each other when far downstream of the flow.

Finally, we reinvestigate the effect of the artificial

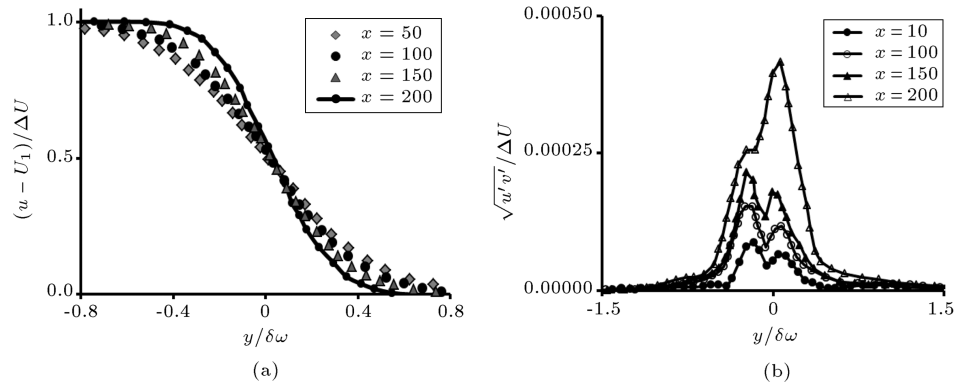

Figure 13. (a) Mean field statistics for u-component velocity. (b) Reynolds stress distribution.

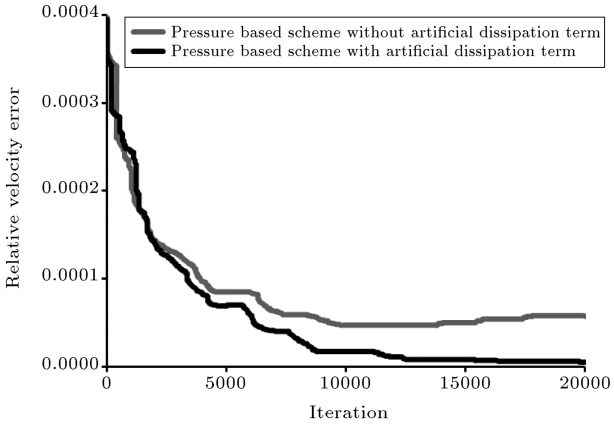

Figure 14. Effect of artificial dissipation term ($\varepsilon_x = \varepsilon_y = 7$) in numerical convergence of the time-dependent mixing layer flow at Re = 300 using pressure based scheme.

dissipation term in simulating a time-dependent mixing layer flow using a pressure based scheme. Figure 14 compares the convergence of the proposed scheme with and without using the artificial dissipation term. Clearly, results highlight the positive effect of the artificial dissipation term on the convergence of the solution.

4. Conclusion

A finite volume formulation of LBM is derived, based on a cell centered discretization scheme on structured tessellation. For this purpose, pressure based correction factors, as well as the artificial dissipation term, were used to improve stability. Also, consistent boundary conditions have been described. The method was validated by simulating the time-dependent flow over a circular cylinder and a forced mixing layer flow. Comparing the results to the well-documented numerical/experimental data in the literature, good agreement was observed. It was also shown that the scheme is robust and promising in simulating time-dependent flows.

References

1. McNamara, G.R. and Zanetti, G. "Use of the Boltzmann equation to simulate lattice gas automata". *J. Phys. Rev. Let.*, **61**, pp. 2332-2335 (1988).
2. Succi, S. (2001) *The Lattice Boltzmann Equation for Fluid Dynamics and Beyond*, Oxford University Press, Oxford, UK.
3. Yu, D., Mei, R. and Luo, L.S. "Viscous flow computations with the method of lattice Boltzmann equation", *Prog. Aero. Sci.*, **39**, pp. 329-367 (2003).
4. Qian, Y.H., D'Humieres, D. and Lallemand, P. "Lattice BGK models for navier-stokes equation", *Europhys. Lett.*, **17**(6), pp. 479-484 (1992).
5. Succi, S., Karlin, I.V. and Chen, H. "Role of the H-theorem in lattice Boltzmann hydrodynamic simulations", *Rev. Mod. Phys.*, **74**, pp. 1203-1220 (2002).
6. D'Humières, D. "Generalized lattice Boltzmann equations", *Prog. Aeronaut. Astronaut.*, **159**, pp. 450-458 (1992).
7. Lallemand, P. and Luo, L.S. "Theory of the lattice Boltzmann method: dispersion, dissipation, isotropy, galilean invariance and stability", *Phys. Rev. E*, **61**, pp. 6546-6562 (2000).
8. D'Humierès, D. "Multiple-relaxation-time lattice Boltzmann models in three dimensions", *Phil. Trans. R. Soc. Lond. A*, **360**, pp. 437-451 (2002).
9. Geier, M.C. "Ab initio drivation of the cascade lattice Boltzmann", PhD Thesis, University of Freiburg, Freiburg, Germany (2006).
10. Ricot, D., Marié, S., Sagaut, P and Bailly, C. "Lattice Boltzmann method with selective viscosity filter", *J. Comput. Phys.*, **228**, pp. 4478-4490 (2009).
11. Ansumali, S. and Karlin, I.V. "Stabilization of the lattice Boltzmann method by the Htheorem: A numerical test", *Phys. Rev. E*, **62**(6), pp. 7999-8003 (2002).
12. Ansumali, S. and Karlin, I.V. "Single relaxation time model for entropic lattice Boltzmann methods", *Phys. Rev.* E, **65**, 056312 (2002).
13. Ansumali, S., Karlin, I.V. and Ottinger, H.C. "Minimal entropic kinetic models for hydrodynamics", *Europhys. Lett.*, **63**(6), pp. 798-804 (2003).

14. Chikatamarla, S., Ansumali, S. and Karlin, I.V. "Entropic lattice Boltzmann models for hydrodynamics in three dimensions", *Phys. Rev. Lett.*, **97**(1), 010201 (2006).

15. Filippova, O. and Hanel, D. "Grid refinement for lattice-BGK models", *J. Comput. Phys.*, **147**(1), pp. 219-228 (1998).

16. Tolke, J., Freudiger, S. and Krafczyk, M. "An adaptive scheme using hierarchical grids for lattice Boltzmann multi-phase flow simulations", *Comput. Fluids*, **35**(8/9), pp. 820–830 (2006).

17. He, X., Luo, L.S. and Dembo, M. "Some progress in lattice Boltzmann method: Part I. Nonuniform mesh grids", *J. Comput. Phys.*, **129**, pp. 357-363 (1996).

18. He, X., Luo, L.S. and Dembo, M. "Some progress in lattice Boltzmann method: Enhancement of Reynolds number in simulations", *Physica A*, **239**, pp. 276-285 (1997).

19. Rohde1, M., Kandhai, D., Derksen, J.J. and Van den Akker, H.E.A. "A generic, mass conservative local grid refinement technique for lattice-Boltzmann schemes", *Int. J. Numer. Meth. Fluids*, **51**, pp. 439-468 (2006).

20. Bouzidi, M., D'Humieres, D., Lallemand, P. and Luo, L.S. "Lattice Boltzmann equation on a two-dimensional rectangular grid", *J. Comput. Phys.*, **172**, pp. 704-717 (2001).

21. Shu, C., Niu, X.D. and Chew, Y.T. "Taylor-series expansion and least-squares-based lattice Boltzmann method: two-dimensional formulation and its applications", *Phys. Rev. E.*, **65**, 036708 (2002).

22. Nannelli, F. and Succi, S. "The lattice Boltzmann equation on irregular lattices", *J. Stat. Phys.*, **68**, pp. 401-407 (1992).

23. Peng, G., Xi, H., Duncan, C. and Chou, S-H. "Finite volume scheme for the lattice Boltzmann method on unstructured meshes", *Phys. Rev. E.*, **59**, pp. 4675-4682 (1999).

24. Stiebler, M., Tolke, J. and Krafczyk, M. "An upwind discretization scheme for the finite volume lattice Boltzmann method", *Comput. Fluids*, **35**, pp. 814-819 (2006).

25. Ubertini, S. and Succi, S. "Recent advances of lattice Boltzmann techniques on unstructured grids", *Prog. Comput. Fluid Dyn.*, **5**(1/2), pp. 85-96 (2005).

26. Zarghami, A., Ubertini, S. and Succi, S. "Finite volume lattice Boltzmann modeling of thermal transport in nanofluids", *Comput. Fluids*, **77**, pp. 56-65 (2013).

27. Hirsch, C. "Numerical computation of internal and external flows", *Fundamentals of Numerical Discretization* **I**, John Wiley, Chichester, UK (1988) .

28. Razavi, S.E., Ghasemi, J. and Farzadi, A. "Flux modeling in the finite volume lattice Boltzmann approach", *Int. J. Comput. Fluid D.*, **23**(1), pp. 69-77 (2009).

29. Zarghami, A., Maghrebi, M.J., Ubertini, S. and Succi, S. "Modeling of bifurcation phenomena in suddenly expanded flows with a new finite volume lattice Boltzmann method", *Int. J. Mod. Phys. C*, **22**(9), pp. 977-1003 (2011).

30. Tanehill, J.C., Anderson, D.A. and Pletcher, R.H. *Computational Fluid Mechanics and Heat Transfer*, pp. 101-126, Taylor & Francis, USA (1997).

31. Zarghami, A., Maghrebi, M.J., Ghasemi, J. and Ubertini, S. "Lattice Boltzmann finite volume formulation with improved stability", *Commun. Comput. Phys.*, **12**(1), pp. 42-64 (2012).

32. Coutanceau, M. and Bouard, R. "Experimental determination of the main features of the viscous flow in the wake of a circular cylinder in uniform translation. Part 1. Steady flow. Part 2. Unsteady flow", *J. Fluid Mech*, **79**, pp. 231-256 (1977).

33. Dennis, S.C.R. and Chang, G.Z. "Numerical solutions for steady flow past a circular cylinder at Reynolds numbers up to 100", *J. Fluid Mech.*, **42**, pp. 471-489 (1970).

34. Nieuwstadt, F. and Keller, H.B. "Viscous flow past circular cylinders", *Comput. Fluids*, **1**, pp. 59-71 (1973).

35. He, X. and Doolen, G. "Lattice Boltzmann method on curvilinear coordinates system: Flow around a circular cylinder", *J. Comput. Phys.*, **134**, pp. 306-315 (1997).

36. Patil, D.V. and Lakshmisha, K.N. "Finite volume TVD formulation of lattice Boltzmann simulation on unstructured mesh", *J. Comput. Phys.*, **228**, pp. 5262-5279 (2009).

37. Fornberg, B. "A numerical study of steady viscous flow past a circular" *J. Fluid Mech.* **101**, pp. 583-587 (1980).

38. Calhoun, D. "A Cartesian grid method for solving the two-dimensional streamfunction-vorticity equations in irregular regions", *J. Comput. Phys.*, **176**(2), pp. 231-275 (2002).

39. Ye, T., Mittal, R., Udaykumar, H. and Shyy, W. "An accurate cartesian grid method for viscous incompressible flow with complex immersed boundaries", *J. Comput. Phys.*, **156**, pp. 209-240 (1999).

40. Ubertini, S., Succi, S. and Bella, G. "Lattice Boltzmann schemes without coordinates", *Phil. Trans. R. Soc. Lond. A*, **362**, pp. 1763-1771 (2004).

41. Ding, H., Shu, M. and Ca, Q.D. "Application of stencil-adaptive finite difference method to incompressible viscous flows with curved boundary", *Comput. Fluids*, **36**, pp. 786-793 (2007).

42. Liu, C., Zheng, X. and Sung, S.H. "Preconditioned multi-grid methods for unsteady incompressible flows", *J. Comput. Phys.*, **139**, pp. 35-57 (1998).

43. Braza, M., Chassaing, P. and Ha Minh, H. "Numerical study and physical analysis of the pressure and velocity fields in the near wake of a circular cylinder", *J. Fluid Mech.*, **165**, pp. 79-130 (1998).

44. Persillon, H. and Braza, M. "Physical analysis of the transition to turbulence in the wake of a circular cylinder by three-dimensional Navier-Stokes simulation", *J. Fluid Mech.*, **365**, pp. 23-88 (1998).

45. Karniadakis, G.M. and Triantafyllou G.S. "Three-dimensional dynamics and transition to turbulence in the wake of bluff objects", *J. Fluid Mech*, **238**, pp. 1-30 (1992).

46. Thompson, M., Hourigan, K. and Sheridan J. "Three-dimensional instabilities in the wake of a circular cylinder", *Experimental Thermal and Fluid Science*, **12**, pp. 190-196 (1996).

47. Williamson, C.H.K. "Defining a universal and continuous Strouhal-Reynolds number relationship for the laminar vortex shedding of a circular cylinder", *Phys. Fluids*, **31**(10), pp. 2742- 2744 (1998).

48. Schlichting, *Boundary Layer Theory*, Springer (2005).

49. Lowery, P.S. and Reynolds, W. "Numerical simulation of spatially developing forced plane mixing layer", NASA Technical Report NCC2-015, USA (1986).

50. Townsend, A.A.R. *The Structure of Turbulent Shear Flow*, Cambridge University Press, Cambridge, UK (1956).

51. Oster, D. and Wygnanski, I. "The forced mixing layer between parallel streams", *J. Fluid. Mech.*, **123**, pp. 91-99 (1982).

52. Maghrebi, M.J. and Zarghami, A. "DNS of forced mixing layer", *Int. J. Numer. Anal. Mod.*, **7**(1), pp. 173-193 (2010).

Biographies

Ahad Zarghami obtained a PhD degree in 2012 from Shahrood University of Technology, Shahrood, Iran, and is Assistant Professor in the Department of Engineering at the Fars Science and Research Branch of the Islamic Azad University. He is currently undertaking a post-doctoral fellowship in H2CU Honors Center of Italian Universities, La Sapienza University of Rome, Italy. His research interests include computational fluid dynamics, lattice Boltzmann method, nanofluids and heat transfer.

Pourya Omidvar obtained a PhD degree, in 2010, from the University of Manchester, UK, under the supervision of Prof. Peter K. Stansby and Dr. Benedict D. Rogers mostly focused on extreme waves loading on wave-energy devices and wave-body interactions. He has been one of the contributors for the open-source code SPHysics. The code SPHysics, which is a SPH (Smoothed Particle Hydrodynamics) code, has been developed jointly in Manchester in cooperation with reputed institutions in the world. He was also employed by EPFL, Switzerland in 2010 and 2011. and is currently Assistant Professor at the State University of Yasouj, Iran. His research interests include numerical modeling, meshless and particle methods, Smoothed-Particle Hydrodynamics (SPH), Lattice Boltzmann Method (LBM), free-surface flow and fluid-structure interaction.